APL Photonics

RESEARCH ARTICLE | AUGUST 06 2024

Propagation of broadband mid-infrared optical pulses in atmosphere

Special Collection: Mid-IR Photonics

Christian Hensel ; Lenard Vamos ; Igor Tyulnev ; Ugaitz Elu ; Jens Biegert

APL Photonics 9, 080801 (2024)
https://doi.org/10.1063/5.0218225

AIP Publishing

Propagation of broadband mid-infrared optical pulses in atmosphere

Cite as: APL Photon. 9, 080801 (2024); doi: 10.1063/5.0218225
Submitted: 9 May 2024 • Accepted: 21 July 2024 •
Published Online: 6 August 2024

Christian Hensel,[1] Lenard Vamos,[1] Igor Tyulnev,[1] Ugaitz Elu,[2] and Jens Biegert[1,3,a)]

AFFILIATIONS

[1] ICFO–Institut de Ciencies Fotoniques, The Barcelona Institute of Science and Technology, 08860 Castelldefels, Barcelona, Spain
[2] FHI-MPG–Fritz-Haber-Institut der Max-Planck-Gesellschaft, Faradayweg 4-6, 14195 Berlin, Germany
[3] ICREA, Pg. Lluís Companys 23, 08010 Barcelona, Spain

Note: This paper is part of the APL Photonics Special Topic on Mid-IR Photonics.
[a)] **Author to whom correspondence should be addressed:** jens.biegert@icfo.eu

ABSTRACT

We study and describe the reshaping of ultrashort and broadband mid-IR optical pulses in an ambient atmosphere. While all pulse propagation undergoes dispersion and absorption, which causes pulse reshaping, the effects are strongly pronounced for broadband radiation in the mid-IR due to the orders of magnitude greater oscillator strengths of molecular constituents of our atmosphere. A noticeable macroscopic impact is a transition of the measured autocorrelation function from squared hyperbolic secant to Lorentzian, which we fully explain based on pulse propagation, including molecular free induction decay. Electro-optical sampling directly reveals the light wave response to atmospheric molecular free induction decay, and a Kramers–Kronig-based propagation model thoroughly explains the observation. The findings are essential for applications in sensing, standoff detection, high-energy pulse propagation, and energy delivery.

I. INTRODUCTION

Mid-IR optical pulses[1,2] are crucial for modern science and for applications due to the scaling of the mid-IR interaction with matter, the much higher absorption cross section, and the anomalous dispersion. Examples are the ultrasensitive detection[3–5] of volatiles[5–7] in biochemistry, agriculture,[8] environment,[9,10] or medicine.[11–17] The interplay of anomalous dispersion with linear or nonlinear propagation offers opportunities to process materials or to exploit soliton dynamics for pulse shaping,[18,19] communication,[20,21] or energy delivery.[22,23] Furthermore, the ponderomotive scaling of light–matter interaction [24–27] provides fascinating avenues for attosecond science,[28–32] x-ray generation,[33–39] and plasma and particle physics.[40–42] However, the extensive oscillator strengths, the multitude of absorption lines and their phase profiles also present a tremendous challenge since pulse propagation is massively altered compared to the near-IR or visible, and a reliable prediction of achievable target parameters requires intricate modeling. Compared to the near-IR, the absorption lines are far more intricate due to the pronounced vibrational and rotational degree of freedom of molecules, which is temperature, pressure, and humidity dependent. Clearly, propagation effects can be mitigated by removing the humidity of air or a vacuum environment, but at the expense of experimental complication. Such a solution is entirely impractical when long-distance target energy delivery is warranted for applications such as remote sensing with light detection and ranging (LIDAR)[43] or laser-induced breakdown spectroscopy (LIBS).[44]

Previous approaches to describe linear propagation with analytical models[45] or simplified dispersion formulas[46] were only successful for narrowband light and do not describe the propagation of ultrashort mid-IR pulses,[47] which will involuntarily lead to strong pulse modulation.[48] The increased interest in mid-IR LIDAR and LIBS applications has even prompted studies on nonlinear atmospheric propagation of intense mid-IR pulse filaments.[49–52] The theoretical description relies on extensive data from the HITRAN database,[53,54] but most models do restrict the degrees of freedom. For instance, including linear vibrational motion works well for CO_2,[55–57] N_2,[48] or CH_3CN,[58] but even including the simple fundamental bending mode of the top-hat H–O–H molecule at 47.8 THz[59] results in a far more complex spectrum;[57] see Fig. 1.

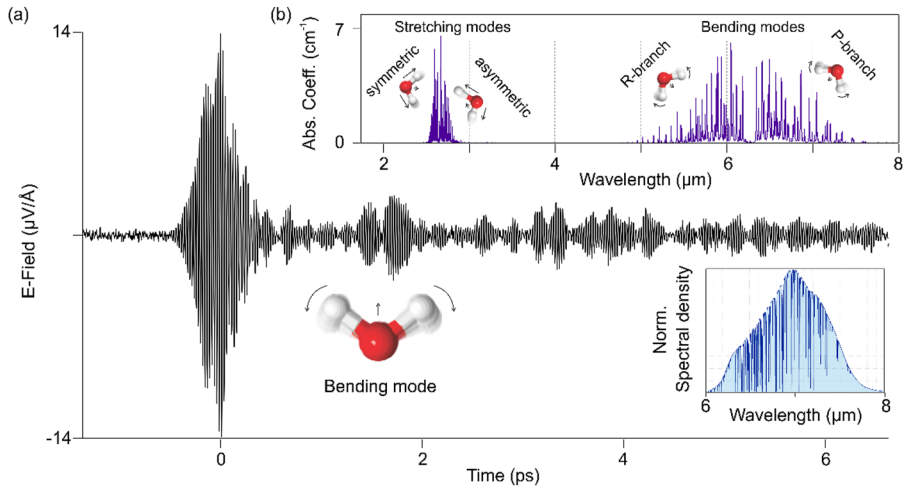

FIG. 1. (a) Measured mid-IR electric field after 2.5 m of propagation in the atmosphere. The water vibrational mode is illustrated close to the induced echo, and the retrieved mid-IR spectrum is shown in the inset. (b) Water vibrational mode induced absorption spectrum.

Another challenge is high-precision pulse characterization in the mid-IR.[60] For instance, a simple intensity autocorrelation lacks the required sensitivity to detect background or temporal pedestals, and it is ambiguous as it represents a large class of pulse shapes.[61] Thus, we employ electro-optical sampling (EOS)[2,62] to investigate why the hyperbolic secant pulse envelope from a mode-locked laser modifies to a Lorentzian upon propagation through the atmosphere.[63–65]

In this work, we build on our recent study,[62] which demonstrated the high spectral and phase sensitivity of our EOS scheme in detecting water absorption signatures during mid-IR field atmospheric propagation. We now explore the impact of water absorption lines on ultrashort mid-IR pulses within the 6–8 μm wavelength range and present a robust model that accurately predicts the electric field distortions caused by atmospheric propagation. The strong correlation between our measurements and simulations confirms that water is the predominant absorption component in this wavelength range. This finding is consistent with the absorption cross sections of various atmospheric elements listed in the HITRAN database.[53,54]

The methodology for generating and field-resolved detection of mid-IR pulses is outlined in Ref. 62. The ultrashort broadband mid-IR pulses are produced in a BGGSe nonlinear crystal through differential frequency generation (DFG), combining the 1.56 and 2.0 μm femtosecond outputs from a multicolor Er:fiber laser. These mid-IR pulses, with a pulse energy of 21 pJ and a duration of 91 fs, are separated from the near-infrared pulses, collimated to ~2 mm in diameter, and propagated a few meters in the air to study their atmospheric propagation. The 1.56 μm pulses, post-DFG, are recycled to generate the sampling pulses required for field-resolved EOS detection. A normal dispersion solid core photonic crystal fiber broadens the 1.56 μm pulses after the DFG process, and a pair of fused silica wedges compress the near-infrared pulses down to 20 fs.[62] By measuring the polarization change induced by the distorted mid-IR pulses in the near-infrared pulses within a 30 μm thin GaSe crystal, we can achieve field-resolved detection of the distorted mid-IR pulses and measure frequency- and time-resolved absorption lines with extremely high sensitivity.

II. DESCRIPTION OF MID-IR ELECTRIC FIELD PROPAGATION IN THE ATMOSPHERE

Humidity significantly influences the propagation of ultrashort pulses in the atmosphere. To comprehend how these pulses reshape during propagation, we have devised a numerical model based on Kramers–Kronig transformations and the HITRAN database. This model accurately mimics the distortions caused by water molecules, allowing us to quantify water absorption cross sections. Considering factors such as humidity, temperature, pressure, path length, and air composition, we calculate linear dispersion and absorption. Using EOS, we compare our simulations with mid-IR electric-field waveforms. Interactions between mid-IR electric fields and molecules result in resonant absorption and re-emission of radiation, generating interference, sometimes called dark waves.[57] We depict the vibrational modes of atmospheric water, showing both the distorted spectrum and the electric field of mid-IR pulses post-atmospheric propagation. Quantum mechanically, molecules rephase upon interaction, producing forward-scattered light pulses or photon echoes.[66] Rephasing, periodic for linear molecules such as CO_2, becomes more complex for anisotropic top-hat molecules such as water.

Our model replicates the field distortions caused by water molecules using Kramers–Kronig transformations, HITRAN-derived [53,67–70] water absorption cross sections, and Hartmann–Tran absorption line profiles for improved accuracy.[69] First, the imaginary part of the complex refractive index is calculated from HITRAN. Here, we have used the Hartmann–Tran profiles to consider second-order effects such as molecular collisions, which enhance the accuracy compared to Voigt profiles. Then, the Kramers–Kronig (KK) transformations are applied to determine the real part of the complex refractive index.[70] The complex dielectric function is obtained for N_2: 78.084%, O_2: 20.946%, CO_2: 0.0413%,

O_3: 0.01%, and CH_4: 0.000 16% and weighted with the corresponding ratios. Afterward, the complex dielectric function is reduced by a weighting factor corresponding to the partial pressure of the water vapor content, calculated from the vapor-pressure equation[71] $\ln\left(\frac{p_\sigma}{p_c}\right) = \frac{T_c}{T}\left(a_1\vartheta + a_2\vartheta^{1.5} + a_3\vartheta^3 + a_4\vartheta^{3.5} + a_5\vartheta^4 + a_6\vartheta^{7.5}\right)$, where p_σ is the vapor-pressure and p_c and T_c are the pressure and temperature at the critical point, respectively. $\vartheta = 1 - T/T_c$ and a_i are the empiric adjustable parameters given in Ref. 71. Once the complex dielectric function is calculated for the correct humidity, we describe the complex electrical field propagation in the spectral domain $E(\omega, d) = E(\omega, 0)e^{i\frac{\omega}{c}\sqrt{\varepsilon(\omega)}d}$, with $E(\omega, 0)$ being the input electrical field amplitude and the spectral phase being included as an exponential containing the corresponding complex dielectric function $\varepsilon(\omega)$, the propagation length d, and the speed of light c. Due to the extremely low peak intensity of the propagating mid-IR pulses (~0.01 MW/cm^2), the free space propagation in atmospheric air is simulated in the small-signal limit, neglecting nonlinear propagation effects such as optical Kerr and plasma effects.

Our model uses a hyperbolic secant pulse envelope with sinusoidal electric field and is matched to the EOS measurement. The spectral phase is included in the fourth order, resulting in a 124 fs FWHM duration pulse. The simulated ambient conditions are 24 °C at 1 bar atmospheric pressure. Figure 2 shows the results of EOS field-resolved measurements (color) and predicted fields from our pulse propagation model (gray). The model achieves an excellent match with the measurements for an extensive range of parameters, and even the intricate post-pulse electric field structures are well captured. The excellent match provides confidence to assess that, for example, rotational modes of water induce the post pulses, and the temporal position and amplitude of these features directly depend on the water vapor density.

With our atmospheric propagation code validated, we applied the model to investigate the propagation of broadband mid-IR pulses since we previously noticed that a Lorentzian shape best fits the measured autocorrelation (AC) trace in the mid-IR.[64] Note that a Lorentzian function is indicative of lifetime broadening; thus, it elicits the question whether the strong absorption and modulation of the broadband spectrum explain the Lorentzian AC shape since a hyperbolic secant squared (HSS) is expected from the mode-locked laser.[63] To settle the question and address claims that the observed line shape originated from pulse-to-pulse fluctuations rather than strong water absorption, we applied an EOS measurement and our pulse propagation model. Briefly, the input is a 206-fs pulse with spectrum centered at 46.8 THz and residual chirp described by GDD = 840 fs^2 and TOD = −11 520 fs^3, analog to Ref. 64. We simulate propagation in the laser system, equivalent to 3300 mm, for relative humidity ranging from 0% to 40%. Figure 3(a) shows how humidity modifies the AC trace, and Fig. 3(b) provides retrieved FWHM durations from Lorentzian and HSS fits together with the respective mean square error [MSE or second-order moment; Fig. 3(c)]. We find that increasing relative humidity leads to a significant pulse pedestal and, consequently, to reshaping the autocorrelation function. For low humidity values below 20%, the HSS fits best with the smallest MSE. Note that a Lorentzian will also fit with a larger MSE, but without physical justification. Figure 3(c) shows that the MSE is much lower for higher humidity values, above 20%, for the Lorentzian fit. This is in excellent agreement with our previous observation.[64] Note that the Lorentzian fit acquires a higher MSE for humidity values above 35% due to the development of a small pedestal around 1 ps. Based on the simulation, we confirm the previous findings and the physical explanation that the temporal pulse reshaping to a Lorentzian AC is due to increased absorption and dispersion under relative humidity of 40%.

III. MOLECULAR FREE INDUCTION DECAY

The primary pulse shape is affected by absorption from randomly oriented oscillators, with the extended tail of the electro-optic

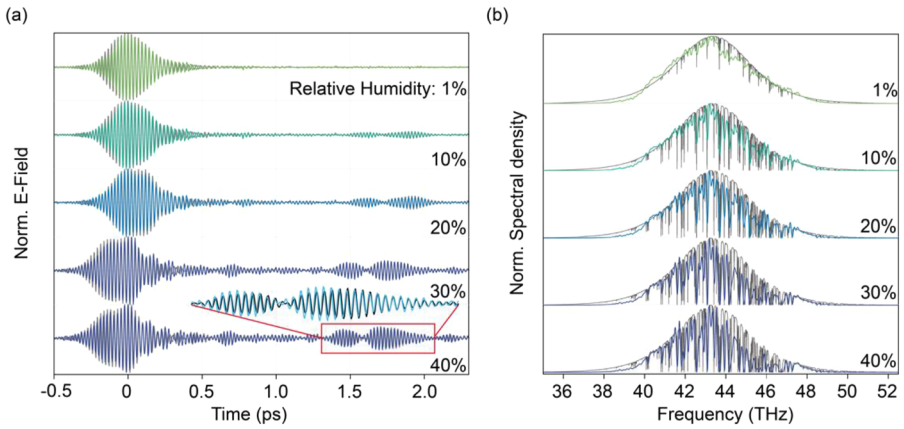

FIG. 2. Comparison between the measured and simulated mid-IR electric field propagation for different atmospheric humidity conditions. (a) Measured mid-IR electric field propagation through 2.5 m with 1% humidity (light green), 10% humidity (dark green), 20% humidity (light blue), 30% humidity (blue), and 40% humidity (dark blue). The corresponding simulated electric fields for 2.5 m propagation at the same humidity values are in gray. The inset shows one of the generated echoes at 40% humidity, measured (light blue) and simulated (black). (b) Spectral densities were retrieved from the measured electric fields (from light green to dark blue) and the corresponding simulated spectra (in gray).

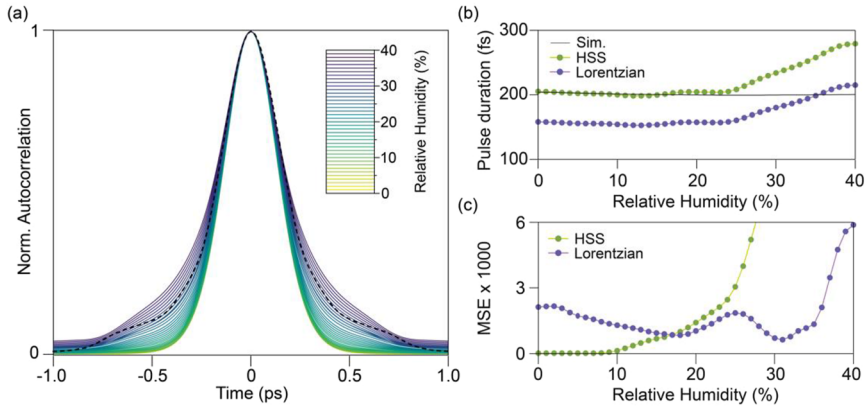

FIG. 3. (a) Simulated autocorrelation traces for relative humidity values from 0% (yellow) to 40% (purple). The black dashed line shows the measured autocorrelation trace in Ref. 64. (b) Simulated autocorrelation FWHM values with Lorentzian fit (purple curve) and HSS shape (green curve). The gray line shows the simulated pulse FWHM values for different relative humidity values. (c) The MSE values were calculated by fitting the Lorentzian (purple dots) and HSS functions (green dots) to the simulated autocorrelation traces shown in (a).

sampling signal primarily stemming from a single polarization component of forward-scattered light. Capturing the omnidirectional energy dispersion of free-induction decay presents a general challenge, and we note that our measurement mainly captures the electric field's polarization on-axis. Figure 4(a) displays spectro-temporal modulation of the propagating pulse and free-induction decay over 10 ps, with the mid-IR electric field frequency shifted to 46.9 THz to maximize water absorption line influence. While temporal delay assessment in linear molecules such as CO_2 relies on quasi-equidistant rotational transitions, the additional rotational freedom in top-hat H_2O molecules impacts the optical field significantly. Nevertheless, high-resolution EOS measurements enable distinguishing individual transitions and exploring complex relaxation processes through time–frequency analysis of echo spectra. Figure 4(a) presents short-time window Fourier transform (STFT) and Wigner–Ville transform (WVT) results. We note that the STFT analysis should be understood as a set of 2D distributions since the spectral resolution depends on the choice of temporal window width. The WVT is shown as it provides the best compromise between spectral and temporal resolution. We first show that

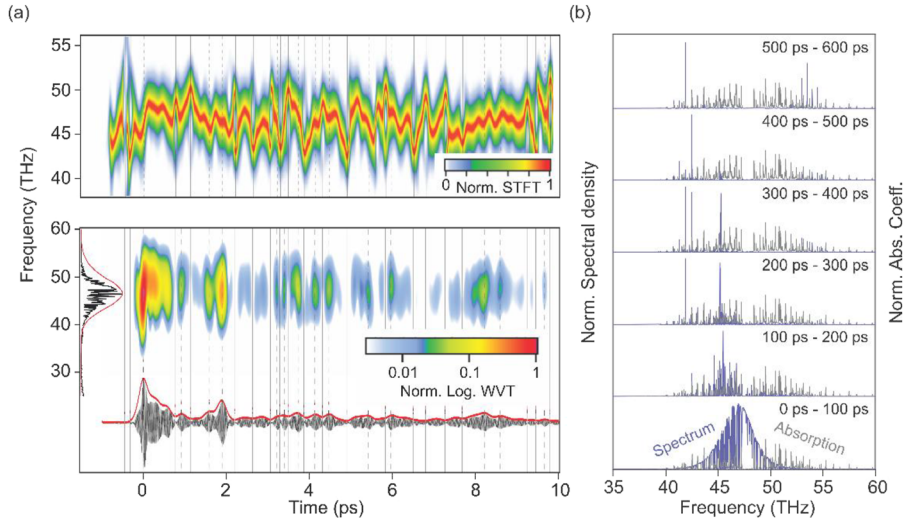

FIG. 4. Temporal and spectral evolution of molecular dynamics. (a) Short-time-windowed Fourier transform (STFT, top) and Wigner–Ville transform (WVT, bottom) of the EOS measurement at 35% humidity. The insets show the marginals (red lines) with the measured (black lines) spectrum and EOS trace. (b) Simulated (blue) spectral content from 0 to 600 ps in steps of 100 ps with water absorption peaks (gray).

spectral distributions with long time windows and high spectral resolution are shown in a longer time range up to 600 ps from simulated data in Fig. 4(b).

For instance, the STFT analysis shows how the center of mass of the spectral distribution shifts as a function of time, emphasizing the chirp of the instantaneous frequency. The normalized STFT gives excellent insights into the time–frequency dependence of the complex couplings and reveals the rotational and modal distribution. In contrast, the WVT barely shows the complex chirp dynamics and energy redistribution within the 43–53 THz energy band, but it reveals rotational and fractional revivals.

IV. SUMMARY

We investigated the propagation of ultrashort and broadband mid-IR radiation in air with a field-resolved technique, capturing both amplitude and phase information. The field-resolved measurement allowed the development of a simple numerical model to accurately describe the propagation, including dispersion and absorption induced by top hat molecules such as water. A time–frequency analysis provides further insights into the free-induction decay and how molecular rovibrational dynamics redistribute energy in the optical field upon propagation. The propagation model explains the previous observation that the macroscopic pulse autocorrelation reshapes to a Lorentzian function arising from the complex free-induction decay. The excellent match between the model and the experimental methodology allows us to accurately predict the atmospheric propagation of ultrashort and broadband infrared radiation. Although we have considered only linear propagation effects, we have demonstrated that water is the dominant component in the atmospheric propagation within the 6–8 μm wavelength range. This information can simplify nonlinear calculations for LIDAR and LIBS applications. The strong agreement between measurements and simulations in the small signal limit paves the way for future studies implementing nonlinear effects.

ACKNOWLEDGMENTS

The authors acknowledge financial support from the European Research Council via ERC Advanced Grant 'TRANSFORMER' (788218) and ERC Proof of Concept Grant 'mini-X' (840010), the European Union's Horizon 2020 for 'PETACom' (829153), FET-OPEN 'OPTOlogic' (899794), PATHFINDER-OPEN 'TwistedNano' (101046424), Laserlab-Europe (871124), Marie Skłodowska-Curie grant no. 860553 ('Smart-X'), MINECO MINECO for 'AttoQM' PID2020-112664GB-100, AGAUR for SGR-2021-01449, 'Severo Ochoa' (CEX2019-000910-S), Fundació Cellex Barcelona, CERCA Programme/Generalitat de Catalunya and the Alexander von Humboldt Foundation for the Friedrich Wilhelm Bessel Prize.

AUTHOR DECLARATIONS

Conflict of Interest

The authors have no conflicts to disclose.

Author Contributions

Christian Hensel: Formal analysis (equal); Methodology (equal); Software (lead); Validation (equal); Visualization (equal); Writing – original draft (equal). **Lenard Vamos**: Conceptualization (equal); Data curation (equal); Formal analysis (equal); Investigation (equal); Methodology (equal); Software (equal); Validation (equal); Visualization (equal); Writing – original draft (equal); Writing – review & editing (equal). **Igor Tyulnev**: Formal analysis (equal); Software (equal); Validation (supporting); Visualization (equal). **Ugaitz Elu**: Data curation (equal); Formal analysis (equal); Investigation (equal); Software (supporting); Validation (equal); Visualization (equal); Writing – review & editing (supporting). **Jens Biegert**: Conceptualization (equal); Funding acquisition (equal); Methodology (equal); Project administration (equal); Resources (equal); Supervision (equal); Writing – review & editing (equal).

DATA AVAILABILITY

The data that support the findings of this study are available from the corresponding author upon reasonable request.

REFERENCES

[1] O. Chalus, P. K. Bates, M. Smolarski, and J. Biegert, "Mid-IR short-pulse OPCPA with micro-Joule energy at 100kHz," Opt. Express **17**, 3587–3594 (2009).
[2] I. Pupeza, D. Sánchez, J. Zhang *et al.*, "High-power sub-two-cycle mid-infrared pulses at 100 MHz repetition rate," Nat. Photonics **9**, 721–724 (2015).
[3] M. Liu, R. M. Gray, L. Costa *et al.*, "Mid-infrared cross-comb spectroscopy," Nat. Commun. **14**(1), 1044 (2023).
[4] S. Vasilyev, A. Muraviev, D. Konnov *et al.*, "Longwave infrared (6.6–11.4 μm) dual-comb spectroscopy with 240,000 comb-mode-resolved data points at video rate," Opt. Lett. **48**, 2273–2276 (2023).
[5] A. S. Kowligy, H. Timmers, A. J. Lind *et al.*, "Infrared electric field sampled frequency comb spectroscopy," Sci. Adv. **5**, 36–38 (2019).
[6] C. W. Van Neste, L. R. Senesac, and T. Thundat, "Standoff spectroscopy of surface adsorbed chemicals," Anal. Chem. **81**, 1952–1956 (2009).
[7] N. A. Macleod, R. Rose, and D. Weidmann, "Middle infrared active coherent laser spectrometer for standoff detection of chemicals," Opt. Lett. **38**, 3708–3711 (2013).
[8] S. Liaghat, S. Mansor, R. Ehsani *et al.*, "Mid-infrared spectroscopy for early detection of basal stem rot disease in oil palm," Comput. Electron. Agric. **101**, 48–54 (2014).
[9] J. Mulrooney, J. Clifford, C. Fitzpatrick, and E. Lewis, "Detection of carbon dioxide emissions from a diesel engine using a mid-infrared optical fibre based sensor," Sens. Actuators, A **136**, 104–110 (2007).
[10] C. S. Goldenstein, V. A. Miller, and R. K. Hanson, "Infrared planar laser-induced fluorescence with a CW quantum-cascade laser for spatially resolved CO_2 and gas properties," Appl. Phys. B **120**, 185–199 (2015).
[11] Y. Wang, Y. Wang, H. Q. Le *et al.*, "Multi-spectral mid-infrared laser stand-off imaging," Opt. Express **13**, 6572–6586 (2005).
[12] J. Nallala, G. R. Lloyd, N. Shepherd, and N. Stone, "High-resolution FTIR imaging of colon tissues for elucidation of individual cellular and histopathological features," Analyst **141**, 630–639 (2016).
[13] M. C. Yu, P. Rich, L. Foreman *et al.*, "Label free detection of sensitive mid-infrared biomarkers of glomerulonephritis in urine using Fourier transform infrared spectroscopy," Sci. Rep. **7**(1), 4601 (2017).
[14] L. C. Pacheco-Londoño, J. R. Castro-Suarez, N. J. Galán-Freyle *et al.*, "Mid-infrared laser spectroscopy applications I: Detection of traces of high explosives on reflective and matte substrates," in *Infrared Spectroscopy—Principles, Advances, and Applications* (IntechOpen, 2019).
[15] I. Pupeza, M. Huber, M. Trubetskov *et al.*, "Field-resolved infrared spectroscopy of biological systems," Nature **577**, 52–59 (2020).
[16] M. R. Treat, S. L. Trokel, V. J. DeFilippi *et al.*, "Mid-infrared lasers for endoscopic surgery. A new class of surgical lasers," Am. Surg. **55**, 81–84 (1989).
[17] Q. Peng, A. Juzeniene, J. Chen *et al.*, "Lasers in medicine," Rep. Prog. Phys. **71**, 056701 (2008).

[18] U. Elu, L. Maidment, L. Vamos *et al.*, "Seven-octave high-brightness and carrier-envelope-phase-stable light source," Nat. Photonics **15**, 277–280 (2021).
[19] M. Hemmer, M. Baudisch, A. Thai *et al.*, "Self-compression to sub-3-cycle duration of mid-infrared optical pulses in dielectrics," Opt. Express **21**, 28095–28102 (2013).
[20] B. Yan, H. Liu, C. Li *et al.*, "Laser-filamentation-assisted 1.25 Gb/s video communication under harsh conditions," Opt Laser. Technol. **131**, 106391 (2020).
[21] H. M. Alyami, V. M. Becerra, and S. Hadjiloucas, "New opportunities for secure communication networks using shaped femtosecond laser pulses inducing filamentation processes in the atmosphere," J. Phys.: Conf. Ser. **472**, 012009 (2013).
[22] E. Lippert, M. W. Haakestad, and H. Fonnum, "High-energy mid-IR laser for defense against heat-seeking missiles," in *SPIE Newsroom* (SPIE, 2014).
[23] J. Hecht, "Scaling down mid-IR laser countermeasures for smaller aircraft," Laser Focus World **50**, 31 (2014).
[24] V. S. Popov, "Energy and angular distributions of photoelectrons in multiphoton ionization," JETP Lett. **70**, 502–507 (1999).
[25] H. R. Reiss, "Limits on tunneling theories of strong-field ionization," Phys. Rev. Lett. **101**, 043002 (2008).
[26] P. Colosimo, G. Doumy, C. I. Blaga *et al.*, "Scaling strong-field interactions towards the classical limit," Nat. Phys. **4**, 386–389 (2008).
[27] B. Wolter, M. G. Pullen, M. Baudisch *et al.*, "Strong-field physics with mid-IR fields," Phys. Rev. X **5**, 021034 (2015).
[28] S. M. Teichmann, F. Silva, S. L. Cousin *et al.*, "0.5-keV soft X-ray attosecond continua," Nat. Commun. **7**, 11493 (2016).
[29] F. Siegrist, J. A. Gessner, M. Ossiander *et al.*, "Light-wave dynamic control of magnetism," Nature **571**, 240–244 (2019).
[30] T. P. H. Sidiropoulos, N. Di Palo, D. E. Rivas *et al.*, "Probing the energy conversion pathways between light, carriers, and lattice in real time with attosecond core-level spectroscopy," Phys. Rev. X **11**, 041060 (2021).
[31] J. Alcalà, U. Bhattacharya, J. Biegert *et al.*, "High-harmonic spectroscopy of quantum phase transitions in a high-Tc superconductor," Proc. Natl. Acad. Sci. U. S. A. **119**, e2207766119 (2022).
[32] J. Freudenstein, M. Borsch, M. Meierhofer *et al.*, "Attosecond clocking of correlations between Bloch electrons," Nature **610**, 290–295 (2022).
[33] T. Popmintchev, M. C. Chen, D. Popmintchev *et al.*, "Bright coherent ultrahigh harmonics in the keV x-ray regime from mid-infrared femtosecond lasers," Science **336**, 1287–1291 (2012).
[34] S. L. Cousin, F. Silva, S. Teichmann *et al.*, "High-flux table-top soft x-ray source driven by sub-2-cycle, CEP stable, 185-μm 1-kHz pulses for carbon K-edge spectroscopy," Opt. Lett. **39**(18), 5383–5386 (2014).
[35] A. R. Attar, A. Bhattacherjee, C. D. Pemmaraju *et al.*, "Femtosecond x-ray spectroscopy of an electrocyclic ring-opening reaction," Science **356**, 54–59 (2017).
[36] B. Buades, D. Moonshiram, T. P. H. Sidiropoulos *et al.*, "Dispersive soft x-ray absorption fine-structure spectroscopy in graphite with an attosecond pulse," Optica **5**(5), 502–506 (2018).
[37] D. Popmintchev, B. R. Galloway, M. C. Chen *et al.*, "Near- and extended-edge X-ray-absorption fine-structure spectroscopy using ultrafast coherent high-order harmonic supercontinua," Phys. Rev. Lett. **120**, 093002 (2018).
[38] K. S. Zinchenko, F. Ardana-Lamas, I. Seidu *et al.*, "Sub-7-femtosecond conical-intersection dynamics probed at the carbon K-edge," Science **371**, 489–494 (2021).
[39] D. Christiansen, M. Selig, J. Biegert, and A. Knorr, "Theory of x-ray absorption spectroscopy: A microscopic Bloch equation approach for two-dimensional solid states," Phys. Rev. Res. **5**, 023002 (2023).
[40] I. V. Pogorelsky, M. N. Polyanskiy, and W. D. Kimura, "Mid-infrared lasers for energy Frontier plasma accelerators," Phys. Rev. Accel. Beams **19**, 091001 (2016).
[41] D. Woodbury, L. Feder, V. Shumakova *et al.*, "Laser wakefield acceleration with mid-IR laser pulses," Opt. Lett. **43**(5), 1131–1134 (2018).
[42] D. Papp, J. C. Wood, V. Gruson *et al.*, "Laser wakefield acceleration with high-power, few-cycle mid-IR lasers," Nucl. Instrum. Methods Phys. Res., Sect. A **909**, 145–148 (2018).
[43] J. Kasparian *et al.*, "White-light filaments for atmospheric analysis," Science **301**, 61–64 (2003).
[44] K. Stelmaszczyk *et al.*, "Long-distance remote laser-induced breakdown spectroscopy using filamentation in air," Appl. Phys. Lett. **85**(18), 3977 (2004).
[45] E. S. Manuilovich, V. A. Astapenko, and P. A. Golovinskii, "Propagation of ultrashort laser pulses in dry and humid air," Atmos. Oceanic Opt. **28**(3), 209–215 (2015).
[46] A. A. Voronin and A. M. Zheltikov, "The generalized Sellmeier equation for air," Sci. Rep. **7**, 46111 (2017).
[47] X. Zhang, A. He, R. Guo, Y. Zhao *et al.*, "A new approach to removing interference of moisture from FTIR spectrum," Spectrochim. Acta, Part A **265**, 120373 (2022).
[48] J. Floß, A. Kamalov, I. S. Averbukh, and P. H. Bucksbaum, "Observation of Bloch oscillations in molecular rotation," Phys. Rev. Lett. **115**(20), 203002 (2015).
[49] B. Shim, S. E. Schrauth, and A. L. Gaeta, "Filamentation in air with ultrashort mid-infrared pulses," Opt. Express **19**, 9118–9126 (2011).
[50] A. Mitrofanov, A. Voronin, D. Sidorov-Biryukov *et al.*, "Mid-infrared laser filaments in the atmosphere," Sci. Rep. **5**, 8368 (2015).
[51] P. Panagiotopoulos, P. Whalen, M. Kolesik, and J. V. Moloney, "Super high power mid-infrared femtosecond light bullet," Nat. Photonics **9**, 543–548 (2015).
[52] H. Liang *et al.*, "Mid-infrared laser filaments in air at a kilohertz repetition rate," Optica **3**, 678–681 (2016).
[53] I. E. Gordon, L. S. Rothman, R. J. Hargreaves *et al.*, "The HITRAN2020 molecular spectroscopic database," J. Quant. Spectrosc. Radiat. Transfer **277**, 107949 (2022).
[54] M. Gebhardt, C. Gaida, F. Stutzki *et al.*, "Impact of atmospheric molecular absorption on the temporal and spatial evolution of ultra-short optical pulses," Opt. Express **23**(11), 13776–13787 (2015).
[55] M. Woerner, A. Seilmeier, and W. Kaiser, "Reshaping of infrared picosecond pulses after passage through atmospheric CO_2," Opt. Lett. **14**(12), 636–638 (1989).
[56] H. Graener, T. Patzlaff, and G. Seifert, "Unusual reshaping of ultrashort mid-IR pulses in atmospheric carbon dioxide," Opt. Commun. **214**(1–6), 297–304 (2002).
[57] A. A. Lanin, A. A. Voronin, A. B. Fedotov, and A. M. Zheltikov, "Time-domain spectroscopy in the mid-infrared," Sci. Rep. **4**, 6670 (2014).
[58] J. Lu, Y. Zhang, H. Y. Hwang *et al.*, "Nonlinear two-dimensional terahertz photon echo and rotational spectroscopy in the gas phase," Proc. Natl. Acad. Sci. U. S. A. **113**(42), 11800 (2016).
[59] D. Paynter, "Measurements and interpretations of the water vapour continuum at near infrared wavelengths," Ph.D. dissertation (The University of Reading, 2008).
[60] P. Bates, O. Chalus, and J. Biegert, "Ultrashort pulse characterization in the mid-infrared," Opt. Lett. **35**(9), 1377–1379 (2010).
[61] R. Trebino, *Frequency-Resolved Optical Gating: The Measurement of Ultrashort Laser Pulses* (Springer US, 2000).
[62] U. Elu, L. Maidment, L. Vamos *et al.*, "Few-cycle mid-infrared pulses from $Baga_2GeSe_6$," Opt. Lett. **45**(13), 3813–3815 (2020).
[63] H. A. Haus, "Mode-locking of lasers," IEEE J. Sel. Top. Quantum Electron. **6**(6), 1173–1185 (2000).
[64] D. Sanchez, M. Hemmer, M. Baudisch *et al.*, "7 μm, ultrafast, sub-millijoule-level mid-infrared optical parametric chirped pulse amplifier pumped at 2 μm," Optica **3**(2), 147 (2016).
[65] U. Elu, T. Steinle, D. Sánchez *et al.*, "Table-top high-energy 7 μm OPCPA and 260 mJ Ho:YLF pump laser," Opt. Lett. **44**(13), 3194–3197 (2019).
[66] I. Coddington, W. C. Swann, and N. R. Newbury, "Time-domain spectroscopy of molecular free-induction decay in the infrared," Opt. Lett. **35**(9), 1395 (2010).
[67] R. V. Kochanov, I. E. Gordon, L. S. Rothman *et al.*, "HITRAN application programming interface (HAPI): A comprehensive approach to working with spectroscopic data," J. Quant. Spectrosc. Radiat. Transfer **177**, 15–30 (2016).

[68]Y. Tan, R. V. Kochanov, L. S. Rothman, and I. E. Gordon, "Introduction of water-vapor broadening parameters and their temperature-dependent exponents into the HITRAN database: Part I—CO_2, N_2O, CO, CH_4, O_2, NH_3, and H_2S," J. Geophys. Res.: Atmos. **124**(21), 11580–11594, https://doi.org/10.1029/2019jd030929 (2019).
[69]N. H. Ngo, D. Lisak, H. Tran, and J. M. Hartmann, "An isolated line-shape model to go beyond the Voigt profile in spectroscopic databases and radiative transfer codes," J. Quant. Spectrosc. Radiat. Transfer **129**, 89–100 (2013).
[70]V. Lucarini, K. E. Peiponen, J. J. Saarinen *et al.*, *Kramers-Kronig Relations in Optical Materials Research* (Springer-Verlag, 2005).
[71]W. Wagner and A. Pruß, "The IAPWS formulation 1995 for the thermodynamic properties of ordinary water substance for general and scientific use," J. Phys. Chem. Ref. Data **31**(2), 387 (2002).